



HAL
open science

Experimental and numerical investigation of drying rate impact on moisture loss, exchange coefficient and drying shrinkage of cement paste

Justin Kinda, Alexandra Bourdot, Laurent Charpin, Sylvie Michel-Ponnelle,
Jean-Luc Adia, Romain Thion, Remi Legroux, Farid Benboudjema

► To cite this version:

Justin Kinda, Alexandra Bourdot, Laurent Charpin, Sylvie Michel-Ponnelle, Jean-Luc Adia, et al.. Experimental and numerical investigation of drying rate impact on moisture loss, exchange coefficient and drying shrinkage of cement paste. *Construction and Building Materials*, 2022, 330, 10.1016/j.conbuildmat.2022.127099 . hal-03722692

HAL Id: hal-03722692

<https://hal.science/hal-03722692>

Submitted on 22 Jul 2024

HAL is a multi-disciplinary open access archive for the deposit and dissemination of scientific research documents, whether they are published or not. The documents may come from teaching and research institutions in France or abroad, or from public or private research centers.

L'archive ouverte pluridisciplinaire **HAL**, est destinée au dépôt et à la diffusion de documents scientifiques de niveau recherche, publiés ou non, émanant des établissements d'enseignement et de recherche français ou étrangers, des laboratoires publics ou privés.



Distributed under a Creative Commons Attribution - NonCommercial 4.0 International License

1 Experimental and numerical investigation of drying
2 rate impact on moisture loss, exchange coefficient and
3 drying shrinkage of cement paste

4 Justin Kinda^{a,b,d,*}, Alexandra Bourdot^b, Laurent Charpin^a,
5 Sylvie Michel-Ponnelle^c, Jean-Luc Adia^a, Romain Thion^a, Remi Legroux^b,
6 Farid Benboudjema^b

7 ^a*EDF R&D, EDF Lab Les Renardières, 77818 Morêt-sur-Loing Cedex, France*

8 ^b*Université Paris-Saclay, ENS Paris-Saclay, CNRS, LMT - Laboratoire de Mécanique
9 et Technologie, 91190, Gif-sur-Yvette, France*

10 ^c*IMSIA, UMR 9219 EDF-CNRS-CEA-ENSTA, 91762 Palaiseau, France*

11 ^d*University of Luxembourg, Laboratory of Solid Structures, 6, Rue Richard
12 Coudenhove-Kalergi, L-1359, Luxembourg*

13 **Abstract**

Assessment of moisture content evolution and drying shrinkage is important for the long-term operation of large concrete structures. This paper evaluates the impact of size and boundary conditions in the prediction of mass loss and drying shrinkage of cement-based materials at ambient temperature. The authors conducted the study on ordinary portland cement paste. The size of specimens spanned from 1 mm to 36 mm. The experiments were performed in environmental SEM, DVS, climatic chamber and saturated salt solutions chambers. The mass loss, as well as drying shrinkage, have been recorded and simulated. The numerical simulations of experimental results show the drying and shrinkage models' ability to take into account size effects, which is important when such models are validated on a thin specimen at laboratory scale for prediction at the structural scale. The drying model is used to discuss in detail the convection exchange coefficient between the material and the environment. A sensitivity study is proposed to find out which type of boundary conditions is the most suitable for drying modelling. The authors then introduce a Biot-type dimensionless number called, Surface Bulk Constant (SBC), to compare the vapour diffusion rate in the air and moisture diffusion rate in the porous medium. Its comparison with the intrinsic permeability shows that it is useless to use a boundary layer condition when the moisture diffusion in the material is

slower than the vapour diffusion in the air, independently of the size of the specimen.

14 *Keywords:* Cement paste, drying rate, size effect, mass loss, surface
15 exchange, drying shrinkage.

16 **1. Introduction**

17 The durability of major pre-stressed structures such as nuclear power
18 plants or large bridges has been a critical topic for many years [1, 13, 19, 8].
19 Since the durability of such structures strongly depends on the level of
20 pre-stress, every phenomenon causing changes of the pre-stress level should
21 be studied [20, 11]. The first of these phenomena is drying [10, 7, 36,
22 6, 5, 17, 27]. Indeed, drying is the primary source of drying shrinkage and
23 drying creep that are essential phenomena occurring in large structures such
24 as nuclear containment buildings or large bridges [31, 13, 29, 46, 44, 64].
25 Moisture variation causes a change in the stresses applied by the fluids
26 occupying the porous space on the solid skeleton of concrete, resulting in
27 macroscopic deformations [23, 75, 71].

28 Moreover, when exposed to drying, gradients of water content ap-
29 pear between the surface and the core of the specimen : the surface of
30 the specimen experiences tensile stresses while its core is under compres-
31 sion [9, 42, 12, 67, 71]. Drying induced stress gradients [15, 32, 14, 57, 72]
32 and incompatibilities between cement paste and aggregates [80, 21, 43, 68]
33 can lead to cracking; the larger the specimen, the larger the moisture gra-
34 dient between the core and the surface of the specimen, the more likely the
35 tensile stress may exceed the tensile strength of the material; and the most
36 likely cracking might occur [69]. Distributed microcracking potentially re-
37 sults in a loss of concrete stiffness and strength [16, 84, 47, 54] and especially
38 increase the penetration of chloride and sulfate in the concrete structures
39 [26]. One of the fundamental goal in this study, is to avoid cracking due
40 drying for the specimens, even for the large ones, by using specific drying
41 process. Hence we will be able to investigate the drying shrinkage of the
42 material free of micro-cracking. In fact, to evaluate the durability of con-
43 crete structures, it is important to be able to predict its drying first [33, 22].

*Corresponding author

Email address: justinkinda4@gmail.com (Justin Kinda)

Preprint submitted to Elsevier

September 13, 2021

44 However, in-situ measurements of the evolution of the water content of the
45 structure can be difficult [2]. Therefore, one solution is to validate the
46 models (drying, shrinkage) on a laboratory scale and then transpose these
47 models to the scale of the structure. However, the difference in size will lead
48 to very different drying kinetics [70], which raises the problem of knowing
49 whether the models integrate these differences in drying kinetics [49].
50 Thus, in order to succeed in the transposition from the laboratory (where
51 samples are small and therefore the drying is fast) to the structure (where
52 drying is very slow), it is necessary to properly take into account the influ-
53 ence of humidity on the delayed deformations and more precisely that of the
54 drying rate. On the one hand, this aspect has not been sufficiently studied,
55 and little literature data exists on the subject. On the other hand, a major
56 difficulty in modelling the drying of small samples at the laboratory scale
57 is related to surface exchange effects.

58 This research aims to contribute to service life prediction and durability
59 assessment by investigating the surface exchange and size effects in the
60 drying process and the impact on drying shrinkage.

61 The first part of this work focuses on the investigation of drying. The
62 water desorption isotherm of the studied material is measured and used as
63 input for the drying model. The modelling strategy adopted in this study
64 is a staggered thermo-hydro-mechanical model [13, 37, 79, 77]. The param-
65 eters of the drying model are identified and used for the prediction of mass
66 loss of specimens of various sizes under different drying conditions. In the
67 case of specimens with small thickness, the surface moisture convection co-
68 efficient is carefully examined to ensure it could be calibrated independently
69 of drying model bulk parameters. The unknown that has been chosen to
70 study the drying process is the saturation degree. Herein, the Richards-Fick
71 drying model was chosen to model the drying process [77]. In the second
72 part, drying shrinkage is studied after the calibration of the drying model.
73 Drying shrinkage is considered to be proportional to the variation of pore
74 relative humidity [25, 11, 8, 58].

75 **2. Experimental method**

76 *2.1. Sample preparation*

77 The studied material is a cement paste. A cement of type CEM I 52.5 N
78 CE CP2 NF Gaurin is used, referring to VERCORS concrete [18, 56]. The
79 main characteristics of cement are presented in tab.1.

Table 1: Chemical composition (in % wt) and density (in g/cm^3)

Density(g/cm^3)	Compound proportion (%)										
	SiO ₂	Al ₂ O ₃	Fe ₂ O ₃	TiO ₂	MnO	CaO	MgO	SO ₃	Na ₂ O	K ₂ O	Cl ⁻
3.19	20.8	4.5	2.3	0.3	0.1	63.2	2.1	3.3	0.16	0.73	0.05

Table 2: Acronyms used to describe specimen geometry and experimental condition

DS	Drying Shrinkage
P2mm	Prism of 2 mm thickness
P500 μ m	Prism of 500 μ m thickness
C36mm	Cylinder of 36 mm diameter
CC	Climatic Chamber
SSS	Saturated Salt Solution ¹
FD	Fast Drying
LCIs	Length Change Isotherm
RH20	20% Relative humidity

80 Unlike in VERCORS concrete formulation, no admixture was added
81 since the water-cement ratio was high enough to facilitate the casting pro-
82 cess. The water-cement ratio is 0.52. All specimens came from different
83 batches following the same mixing process. For each batch, the paste (2
84 L) was mixed with a thick stainless mixing blade of 5 L capacity for 1.5
85 min; then tap water was added (1 min). Finally, for another 1.5 min, the
86 mixer was turned on after the paste was scrapped in the mixer. Specimens
87 were cast in cylindrical moulds of sizes $\phi 36 \times 180$ mm or $\phi 30 \times 40$ mm. The
88 specimens were demolded 24 h later and were placed in hermetic containers
89 at constant room temperature ($T = 20 \pm 1^\circ C$) with a bottle of water inside
90 to prevent desiccation (fig.1.a) for at least 90 days before testing. Small
91 prisms of different thicknesses were obtained by cutting the cylinders with
92 a diamond saw (fig.1.b). The cylinders were kept flooded with water during
93 cutting to avoid temperature rise. The thin prisms were then covered with
94 plastic and aluminium foil to prevent exchange with the environment.

95 The average porosity is 46 % (± 0.6).

96 The abbreviations used to describe the experiments are listed in tab.2.
97 For example, P2mm-ESEM-FD will read: **P**rismatic specimen of **2 mm**
98 thickness in **ESEM**, **F**ast **D**rying. The experimental campaign is summa-
99 rized in tab.3.

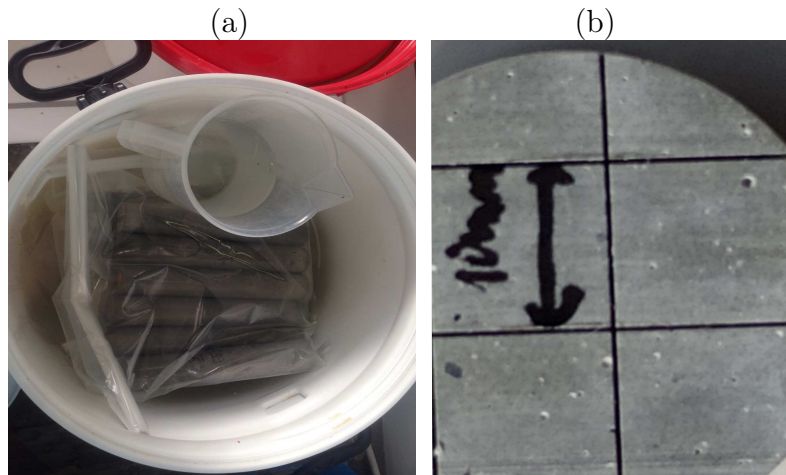


Figure 1: Sample preparation process. (a) Curing under endogenous conditions and (b) sawing of cylinder to obtain prisms of size $10 \times 10 \times 2$ mm.

Table 3: Summary of experimental campaign undertaken on cement paste. DS = Transient Drying Shrinkage; LCI = Length Change Isotherm. SS = Saturated Salt Solution. DVS = Dynamic Vapor Sorption. CAC = Circulating Air Conditioning

Test	Geometry (mm)	mass	DS	LCI	system	DS monitoring
P2mm-ESEM-FD	$10 \times 10 \times 2$	-	✓	-	ESEM	DIC
P1mm-DVS	$10 \times 5 \times 1$	-	✓	-	DVS	-
P500 μ m-CC-LCIs	$10 \times 10 \times 0.5$	-	✓	✓	CC	DIC
P2mm-CC-SD	$10 \times 10 \times 2$	✓	✓	-	CC	DIC
C18-SS-RH80 %	36×180	✓	✓	-	SS	LVDT
C18-SS-RH58 %	36×180	✓	✓	-	SS	LVDT
C18-SS-RH20 %	36×180	✓	✓	-	SS	LVDT
C18-CAC-RH50 %	36×180	✓	✓	-	CAC	-

100 *2.2. Measurements of mass loss*

101 In all tests, the sample dries on all sides. Four distinct mass-loss exper-
 102 iments were performed:

- 103 • Cylinder $\phi 36$ mm diameter exposed to 50% RH in a large room, where
 104 humidity was controlled by a Circulated Air Conditioning (CAC) sys-
 105 tem.

- 106 • Cylinders $\phi 36$ mm in diameter exposed to drying, at 20-58-80 % RH,
107 imposed by saturated salt solutions in small hermetic chambers. Hu-
108 midity was not constant but slowly decreased from an initial value
109 close to the sample initial internal RH, to the target value imposed
110 by the Saturated salt Solution (SSS). This protocol reduces the risk
111 of cracking by drying stress gradient. Mass loss of these cylinders was
112 recorded using a balance of type of KERN with 6200 g capacity and
113 with a precision of 0.1 g.
- 114 • Prism of $1 \times 10 \times 10$ mm geometry, drying at different humidities step
115 using Dynamic Vapor Sorption (DVS). A digital microbalance with 1
116 g total capacity and 0.1 μg of precision is used.
- 117 • Prism of $0.5 \times 10 \times 10$ mm size, drying at different humidity steps con-
118 trolled by a Climatic Chamber (CC). A Mettler Toledo balance type
119 with 220 g of total capacity and 0.01 mg of precision is used.

120 *2.3. Measurement of desorption isotherm*

121 Desorption isotherms are fundamental for the quantification and predic-
122 tion of the behaviour of the material subjected to drying. By definition, it
123 is the water content (or water saturation degree) vs. RH curve. For the
124 last decades, many efforts had been made to characterize it using different
125 techniques with the intent to make it faster and more accurate. Different
126 techniques exist, such as saturated salt solutions [6, 5], volumetric method
127 [55], Dynamic Vapor Sorption method [63].

128 In this study, the desorption isotherm measurement was performed on
129 cement paste on (i) powder obtained by hand grinding and (ii) prism of
130 $1 \times 10 \times 10$ mm, both from a cylinder specimen of 6 months age cured under
131 endogenous conditions. The dynamic Vapor Sorption (DVS) method was
132 used, and the tests were carried out at a temperature of 25°C. This method
133 is quick and has shown to provide compatible results with classical methods
134 such as saturated water solutions of desiccators or climatic chambers [30,
135 76].

136 *2.4. Measurement of drying shrinkage*

137 The drying shrinkage measurements were performed by Digital Image
138 Correlation (DIC) or by Linear Variable Differential Transformer (LVDT)
139 probes:

- 140 • Shrinkage tests in salt solutions environment (C18-SS-RH20, C18-SS-
141 RH58, C18-SS-RH80): axial strain was monitored using three LVDT
142 sensors installed at 120°. The measurement was made on a 10.8 cm
143 basis [41, 50].
- 144 • Shrinkage tests in ESEM and climatic chamber (P2mm-ESEM-FD,
145 P500 μ m-CC-LCIs, P2mm-CC-SD): images are acquired all along with
146 the test duration and analyzed by DIC. For ESEM tests, a backscat-
147 tered electron (BSE) imaging mode was used, while for the latter, a
148 classical optical camera was used. The images are then post-processed
149 by DIC [38] to assess strains [57, 50].

150 3. Model for drying of cementitious materials

151 Drying of cementitious materials is a very complex phenomenon, in-
152 volving permeation, diffusion, adsorption-desorption, and condensation-
153 evaporation [51, 52, 81]. The model used herein is the Richard-Fick model
154 accounting for permeation of liquid and diffusion of water vapour in the
155 porous network of the material [37, 79], using the saturation degree as a
156 primary variable [77]. The main mass balance equation reads Eq.1

$$\frac{\partial S_l}{\partial t} = \nabla(D(S_l)\nabla S_l) \quad (1)$$

157 where D is the global equivalent diffusion coefficient depending non-linearly
158 on liquid water saturation degree (S_l) named saturation hereafter. Under
159 the assumption of constant gas pressure, the global equivalent diffusion
160 coefficient is given by :

$$D(S_l) = \frac{1}{1 - \frac{\rho_v}{\rho_l}} \frac{\partial P_c}{\partial S_l} \left[\frac{K^{eff}(S_l)}{\phi \mu_l} + D^{eff}(S_l) \left(\frac{M_v}{\rho_l RT} \right)^2 P_{vsat} \exp \left(P_c \frac{M_v}{\rho_l RT} \right) \right] \quad (2)$$

161 with ϕ the porosity of the material, K^{eff} the effective permeability of the
162 liquid, D^{eff} the effective gas diffusion coefficient, P_c the capillary pressure.
163 ρ_l , ρ_v , μ_l are respectively the density of the liquid and gas, the dynamic
164 viscosity of the liquid. T is the temperature, and R the perfect gas con-
165 stant. P_{vsat} and M_v are respectively the saturating vapour pressure and the
166 water molar mass. The first term in Eq.2 represents the liquid permeation
167 mechanism and the second term accounts for vapour diffusion.

168 The effective permeability K^{eff} decreases when saturation diminishes.
169 It can be split into the product of two functions $K^{eff}(S_l) = K_0 k_{rl}(S_l)$ [37]:

170 a constant parameter, denoted K_0 , which is the intrinsic permeability of the
 171 material at full saturation, to be identified by inverse analysis on mass loss
 172 experiment; and the relative permeability k_{rl} , given by the Van Genuchten
 173 relation [60],

$$k_{rl} = S_l^{n_k} \left(1 - (1 - S_l^b)^{1/b} \right)^2 \quad (3)$$

174 where n_k is an empirical parameter accounting for the morphology of
 175 the material pore network to be identified by inverse analysis on mass loss.
 176 The second parameter b is the same as used in Van Genuchten's model for
 177 the desorption isotherm, Eq.4

$$P_c(S_l) = a[S_l^{-b} - 1]^{1-1/b} \quad (4)$$

178 where a is a fitting parameter.

179 The gas diffusion D_{eff} dependence on the saturation coefficient is given
 180 by Millington's empirical relation, [81], and reads Eq.5

$$D^{eff}(S_l) = D_0 \cdot \phi^{a_{mq}} (1 - S_l)^{b_{mq}} \quad (5)$$

181 where a_{mq} is interpreted as a reduced porosity to enhance the fact that air
 182 movement within the material encounters more resistance than in case of
 183 free diffusion in the open air for a given temperature. a_{mq} is to be identified
 184 by inverse analysis of mass loss of specimen drying preferably below 20%
 185 RH while b_{mq} and D_0 are set respectively to 4.2 and $10^{-5} \text{ m}^2/\text{s}$ [81].

186 To solve the differential equation of drying, the boundary condition of
 187 Neumann Eq.6 or Dirichlet, Eq.7 is imposed depending on the drying con-
 188 ditions (more details will be given hereafter).

$$j_{x-} = C_s(S_s - S_e) \quad (6)$$

$$S_s = S_e \quad (7)$$

189 Where j_{x-} [$\text{kg}/\text{m}^2/\text{s}$] is the moisture flux toward the environment; S_s and
 190 S_e are respectively the vapor saturation of the specimen surface and that
 191 of surrounding air (considered as saturation of the material at equilibrium
 192 with the relative humidity of the environment); C_s [$\text{kg}/\text{m}^2/\text{s}$] the surface
 193 exchange coefficient.

194 **4. Numerical simulation of drying: model identification, predic-**
 195 **tion and drying rate effect**

196 *4.1. Mesh and Boundary conditions*

197 The meshes used for the simulations are presented in fig.2.

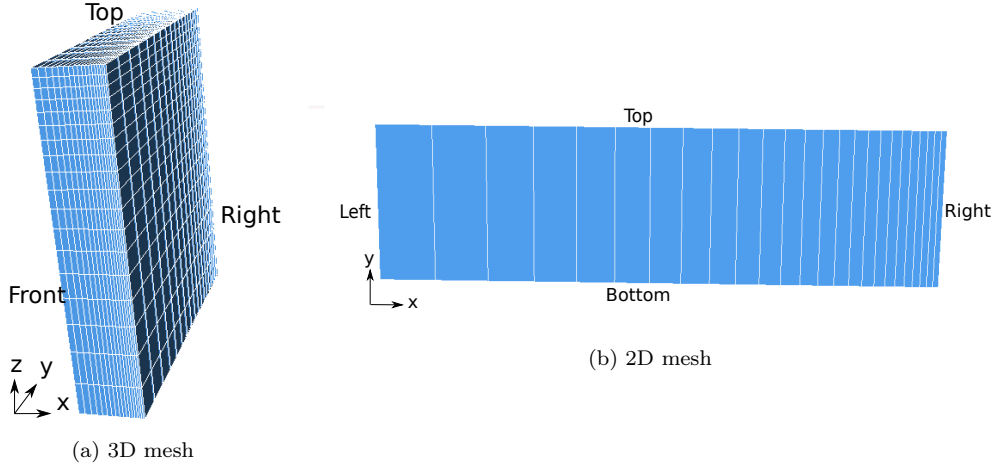


Figure 2: Mesh for drying and drying shrinkage simulations

198 An axisymmetric configuration for cylinders and 1/8 symmetry for pris-
 199 matic samples was used. The discretization and the boundary conditions
 200 are presented in fig.2 and tab.4. Note that a fine mesh was considered at
 201 each drying face of the samples, since gradients may be high and lead to
 202 numerical issues if the mesh is coarse.

Table 4: Boundary conditions corresponding to modelling in fig.2. DSF = Drying Surface, ND = Non Drying Surface.

Face	3D (1/8 symmetry)	2D(axisymmetry)
Top	ND	ND
Bottom	ND	ND
Left	ND	ND
Right	DSF	DSF
Front	ND	
Back	DSF	

203 *4.2. Simulation strategy*

204 The way these experiments are used in the present simulations in order
205 to fulfill the objectives of the study is as follow:

- 206 • C18-CAC-RH50: identification of liquid permeation parameters
207 n_k (Eq.3) and K_0 of Richard model.
- 208 • C18-SS-RH20: identification of vapor diffusion parameter a_{mq} (Eq.5)
209 of Fick model and the exchange coefficient C_s (Eq.6).
- 210 • C18-SS-RH80, DS-C18-SS-RH58, P1mm-DVS: validation of drying
211 model identification by predicting mass loss.
- 212 • P500 μ m-CC-LCIs: determination of drying shrinkage coefficient of
213 the studied material.
- 214 • P2mm-ESEM-FD, DS-P2mm-CC-SD, DS-C18-SS-RH80, DS-C18-SS-
215 RH58: validation of drying and shrinkage model parameters by pre-
216 dicting drying shrinkage for different sizes and rates of drying.

217 *4.3. Identification of desorption isotherm*

218 *4.3.1. Isotherm: from experimental measurement to data for simulations*

219 For finite element simulation purposes, one needs to move from experi-
220 mentally measured water content to an equivalent humidity or saturation,
221 depending on the primary variable needed in drying calculations. Given
222 the drying model, which will be described hereafter, the water content in
223 desorption experiments was converted to saturation. It was achieved by di-
224 viding the water content at equilibrium (mass variation within 24h less than
225 0.01 %) for a given relative humidity by the one at the maximum humidity
226 (max RH) (not necessarily the saturated state). This point is a critical step
227 because the desorption isotherm, in the end, will strongly depend on the
228 chosen max RH. This max RH should be close to 1 as much as possible,
229 with the highest possible confidence on the corresponding water content,
230 which in turn depends on the measurement technique. We have decided to
231 use 95% as max RH, which corresponds to the starting humidity step in our
232 experiment in the DVS apparatus. Measurements performed on powders
233 and solids give very similar results, fig.3.

234 *4.3.2. Fit of desorption curve*

235 First, parameters a and b of capillary pressure (Eq.4) were identified
 236 successfully and the results are displayed in fig. 3. These parameters are
 237 used as input to feed the drying simulation. Because we set the reference
 238 humidity at full saturation to 95% RH, the saturation corresponding to a
 239 relative humidity of 100% is slightly greater than 1 due to the use of max
 240 RH (the saturation is a relative parameter).

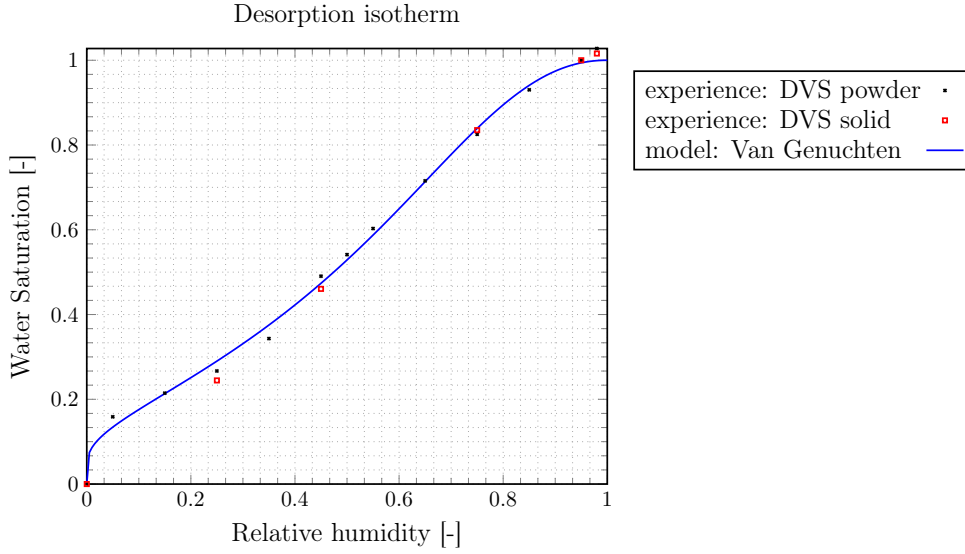


Figure 3: Experimental desorption isotherm of the studied cement paste ($w/c = 0.52$) and numerical fit using Van Genuchten's model ($a = 6.131 \cdot 10^7 \text{ Pa}$, $b = 0.512$)

241 *4.4. Identification of drying parameters*

242 The fixed parameters in drying simulations are reported in tab.5 while
 243 the identified parameters are presented in tab.6.

Table 5: Fixed parameters of drying model

ϕ [-]	ρ_{paste} [kg/m ³]	S_{init} [-]	bmq [-]	P_{vsat} [Pa]	μ_l [Pa.s]	ρ_l [kg/m ³]	ρ_v [kg/m ³]	T [K]	D_0 [m ² .s ⁻¹]
0.465	1870	0.99	4.2	3062	0.001	1000	0.018	293	10^{-5}

244 *4.4.1. Liquid permeation parameters*

245 Second, parameters n_k and K_0 of the liquid permeation term in Eq.2 are
 246 identified using test DS-C18-CAC-RH50 of tab.3; and Dirichlet boundary

247 coefficient. In fact, the air velocity around the sample in this experiment
 248 was high enough to allow for instantaneous evaporation of vapor at the
 249 sample surface. Therefore, imposing a constant saturation condition at the
 250 surface or adopting a very large exchange coefficient is more adapted in this
 251 situation. The fitting of the model to the experimental data is presented in
 252 fig.4.

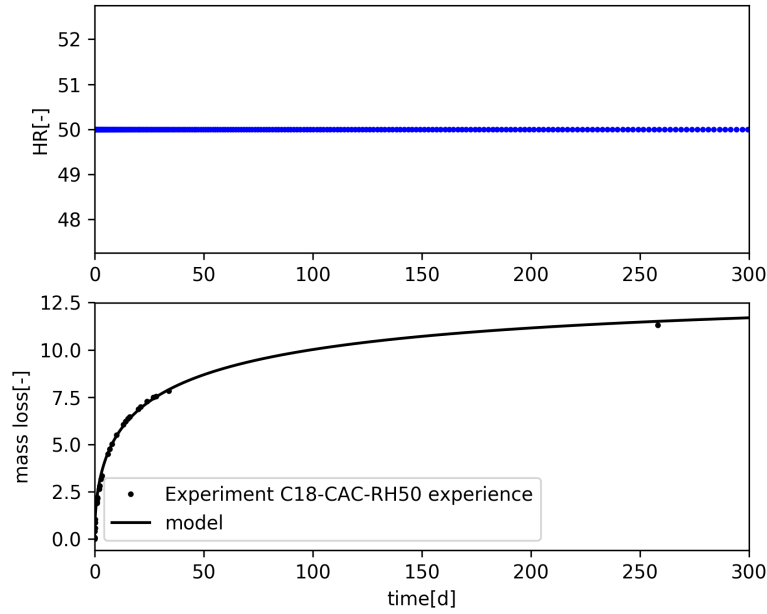


Figure 4: Identification of intrinsic water permeability $K_0 = 1.02 \times 10^{-21} m^2$ and the tortuosity parameter of Van Genuchten's relationship $n_k = 2.52$ on experiment DS-C18-CAC-RH50 (tab.3) performed at 20° C and 50% of relative humidity in the ambient air.

253 *4.4.2. Vapor diffusion parameters*

254 Last the parameter a_{mq} of the vapor diffusion term of Eq.2 is identified
 255 thanks to experiment DS-C18-SS-RH20 presented in tab.3. A type of Neu-
 256 mann boundary conditions was used for this experiment, which means to
 257 identify a supplementary term, called C_s . Results displayed in fig.5 demon-
 258 strate that the identification method is trustworthy.

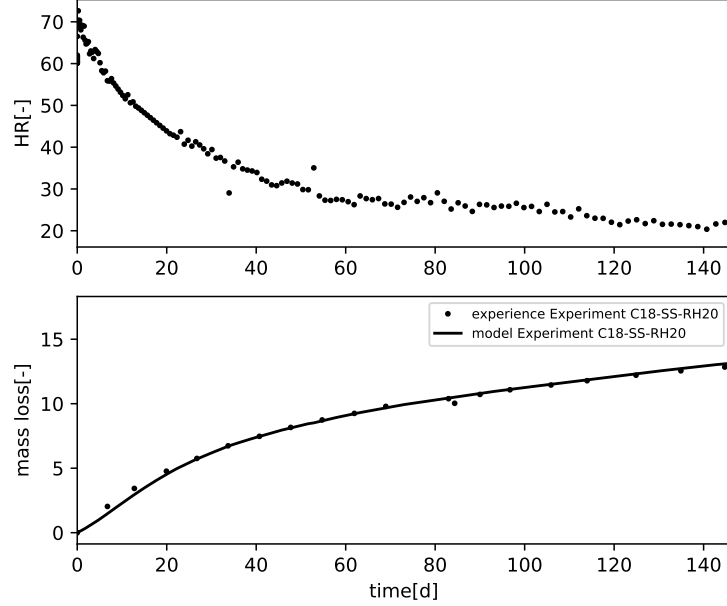


Figure 5: Identification of surface exchange coefficient $C_s = 3.6 \times 10^{-9} [kg.m^{-2}.s^{-1}]$ and vapor diffusion parameter $a_{mq} = 5[-]$ using test DS-C18-SS-RH20 of tab.3

Table 6: Identified parameters of drying model

$K_0 [m^2]$	$n_k [-]$	$a_{mq} [-]$	$C_s [kg.m^{-2}.s^{-1}]$
$1.02 \cdot 10^{-21}$	2.52	5	$3.6 \cdot 10^{-9}$

259 *4.5. Parametric study on the drying model : drying rate and environmental*
 260 *relative humidity level effects*

261 Since models are usually calibrated on laboratory tests and then used
 262 to predict the behavior at the structural level, the size effect of the drying
 263 model is tested. The same parameters identified in the previous section
 264 are used to predict drying moisture loss for different specimen sizes and
 265 different drying conditions.

266 First, the prediction accuracy for different humidity levels is studied
 267 through the simulation of experiments C18-SS-RH80 and C18-SS-RH58 of
 268 tab.3. The numerical results are compared to experimental observations in
 269 fig.6, and the agreement is very satisfactory.

270 The rate of mass loss of test C18-SS-RH20 is also well captured (calibra-
 271 tion was on 140 days while validation is performed over 200 days). Using the

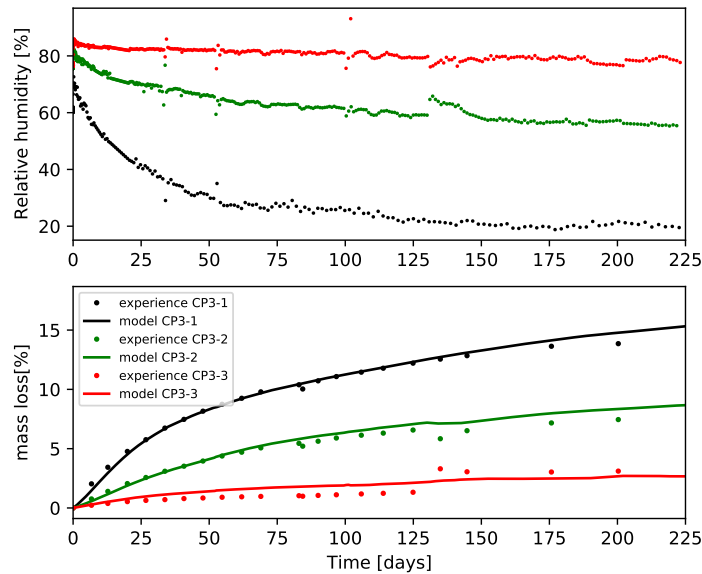


Figure 6: Prediction of mass loss of 36×180 mm cylinders, drying at different relative humidity levels (experiments C18-SS-RH80, C18-SS-RH58 and C18-SS-RH20). Only the first 140 days data from C18-SS-RH20 was used in model identification.

272 identified exchange coefficient for Neumann boundary conditions along with
 273 the Richards model (water permeation) shows us that the kinetics of mass
 274 loss is underestimated even if the equilibrium mass loss is well captured as
 275 expected (fig.7). Therefore, the exchange coefficient is only a reflection of
 276 the indoor drying conditions, not the specimen size nor the model.

277 Second, the independence of parameters of the drying model to drying
 278 kinetics is tested. For that purpose, experiment P1mm-DVS performed on
 279 a prism of 1. mm in thickness (see more description in tab.3) is simulated:
 280 the mass loss is well captured for relative humidity steps A, B and D while
 281 the kinetic is not very well retrieved at steps C and E, fig.8. At, that
 282 lower level of moisture content, the diffusion of vapor is a combination
 283 of different complex mechanisms: molecular diffusion, Knudsen diffusion,
 284 and surface diffusion. Although in our model, we have only considered
 285 the contribution of molecular diffusion to the global diffusion. But for the
 286 lower levels of moisture content, the surface diffusion contribution become
 287 significant, which need to be taken into account to improve our drying
 288 model. Let's stress out that, another strategy for addressing the size effect

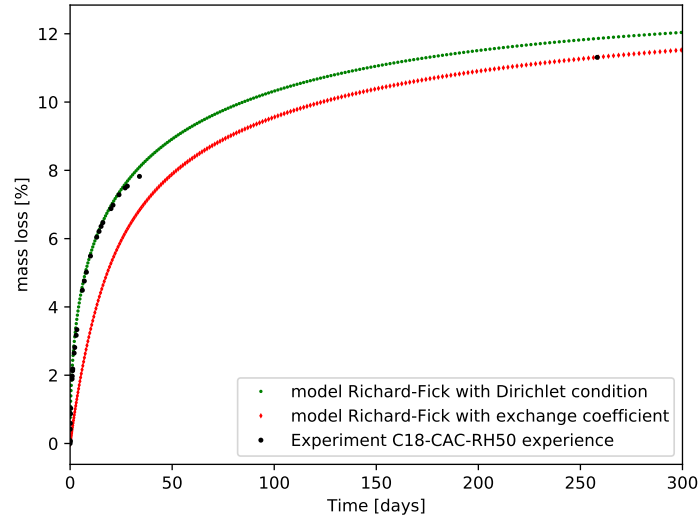


Figure 7: Prediction of mass loss of 36×180 mm cylinder exposed to relative humidity of 50% (test DS-C18-CAC-RH50) using the identified Richards-Fick model: comparison of the two types of boundary conditions, Dirichlet (without exchange coefficient) and Neumann (with the identified exchange coefficient)

289 is to calibrate the model on the thin specimen experiment P1mm-DVS, and
 290 therefore to test the scaling capability of the model on large size specimens.
 291 Unfortunately, experiment P1mm-DVS is not sensitive to surface exchange
 292 due to ventilation at the surface, therefore the model could not be fully
 293 calibrated based on this experiment.

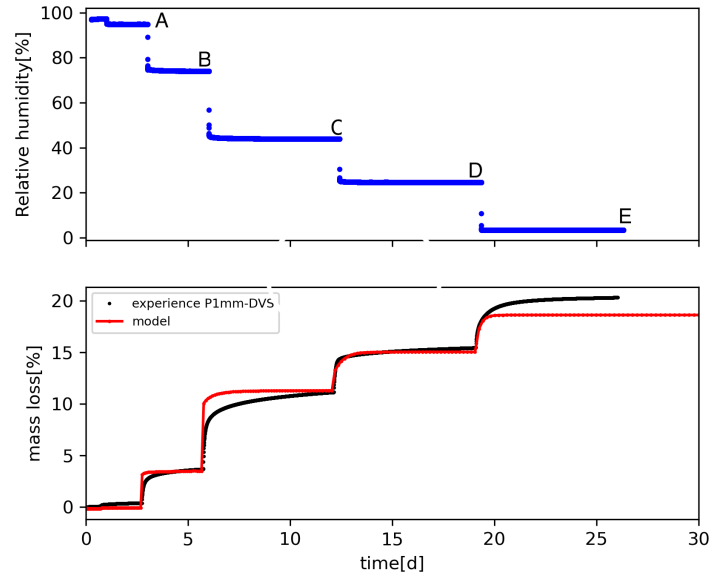


Figure 8: Prediction of mass loss of small prism (P1mm-DVS experiment) of 1 mm drying thickness using the identified models.

294 *4.6. Water content profiles : effect of surface exchange*

295 The prediction of the saturation profiles of the tests on $\phi 36 \times 180$ mm
 296 cylinders is shown in fig.9. It is seen that if surface humidity is imposed
 297 slowly enough (fig.6), the saturation profiles are almost flat, as in the case
 298 of fig.9-(a-b). Conversely, when the relative humidity is imposed rapidly on
 299 the surface (fig.4), the hydric gradients between the core and the surface of
 300 the sample are very strong, especially in the first moments of exposure as
 301 shown in fig.9-(d). For an intermediate drying rate level, the gradients are
 302 less pronounced fig.9-(c) even at the beginning of drying.

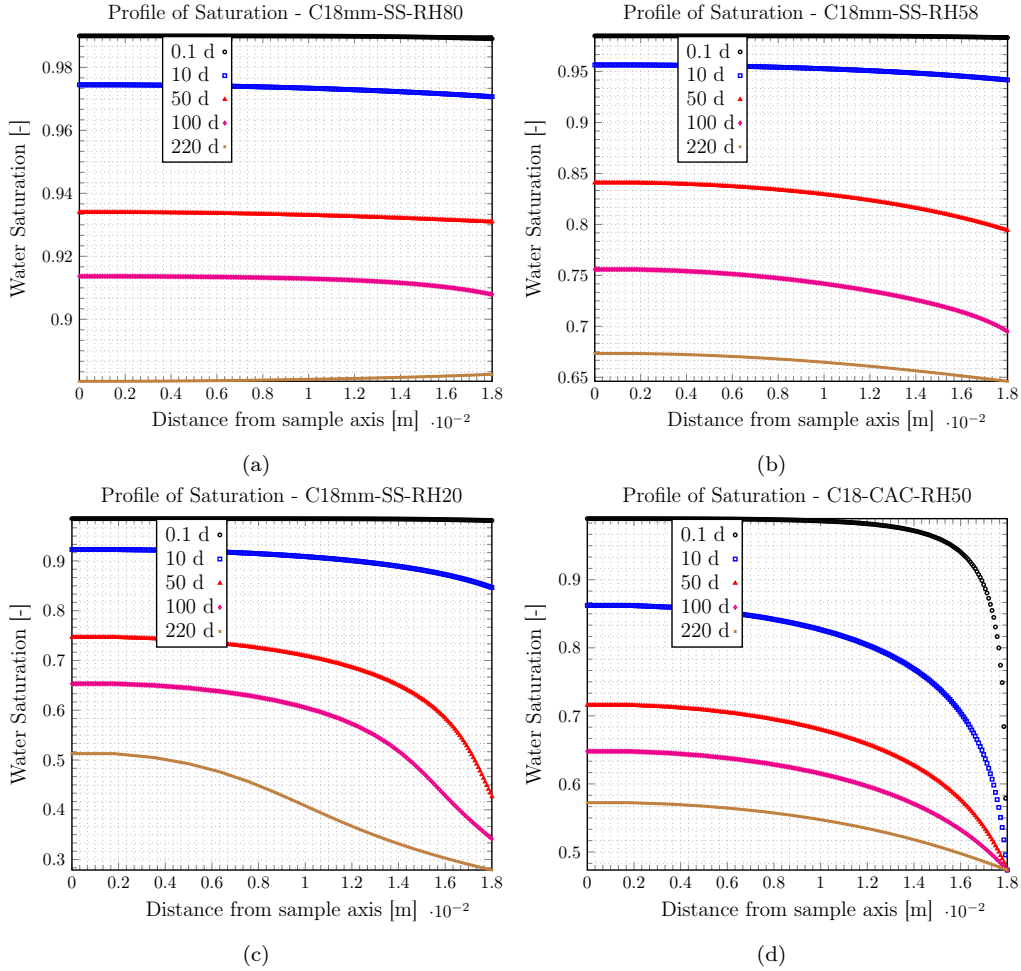


Figure 9: Evolution of water saturation profiles of cylindrical, $\phi 36 \times 180$ mm specimen (tests C18mm-SS-RH80, C18mm-SS-RH60, C18mm-SS-RH20 and C18-CAC-RH50)

303 4.7. Discussion on model identification

304 The drying process was modelled using the Richards-Fick model to
 305 account for liquid permeation and vapour diffusion [52, 81, 37, 79, 77].
 306 Three parameters of the model and additionally surface factor were success-
 307 fully identified using two experiments (DS-C18-CAC-RH50 and DS-C18-SS-
 308 RH20); then we used the model for prediction.

309 Those results suggest that the drying model used herein correctly ac-
 310 counts for the size effect on a large range of humidity. The simulations also
 311 emphasize that the boundary conditions to be used in simulations should
 312 not be only directed by the specimen size but also depend on surround-

313 ing environmental factors. The air velocity around the sample seems to be
 314 the major environmental factor. In fact, even though the specimen of ex-
 315 periments C18-SS-RH20, C18-SS-RH58, C18-SS-RH80 are relatively large
 316 compared to test P1mm-DVS, the air change rate on the specimen surface,
 317 on the contrary, was relatively low because of the use of a hermetic chamber
 318 without any ventilation. Since the air change rate was very low, a moisture
 319 transfer coefficient was then introduced to prescribe a realistic boundary
 320 condition. A low surface exchange coefficient $C_s = 3.6 \cdot 10^{-9} [kg/m^2/s]$
 321 identified on test C18-SS-RH20 was used in this study. The exchange co-
 322 efficient has the beneficial effect of limiting hydric gradients between the
 323 surface and the core of samples, as shown in fig.9. Therefore, it allows re-
 324 ducing the risk of hydric gradient cracking during drying. A further study
 325 on the surface exchange coefficient is undertaken in the following section.

326 5. Investigation on surface moisture transport coefficient

327 5.1. Drying process and surface evaporation

328 Water leaves material through evaporation on its surface. A complete
 329 review of the drying process has been made by [24, 34, 83, 74, 48], and
 330 the attempt here is to recall the main findings. First, when exposed to
 331 drying, the material surface heats up or cools down to equilibrate with the
 332 surrounding atmosphere temperature. Second, it goes up under a constant
 333 drying rate period, during which liquid flow through the porous medium
 334 is fast enough to maintain a wet surface. The evaporation on the surface
 335 proceeds the same way as in the case of flat water surface evaporation as
 336 if the solid phase was absent. Otherwise, this stage is not observed for
 337 materials where the initial water content is low [34]. Last, in the final
 338 stage, the drying rate decreases. In fact, the film of liquid water becomes
 339 discontinuous, the liquid flow slows down, and the material surface may no
 340 longer be fed with water, so it starts to dry (the film water is shrinking)
 341 due to evaporation. As a consequence, the evaporation rate drops.

342 5.2. Boundary conditions with surface convection

343 Let us note $x = 0$ the surface of the material (fig.10) in contact with
 344 the surrounding atmosphere. For the sake of simplicity, we consider herein,
 345 a unidirectional drying hypothesis at a surface defined by its normal x^+ .
 346 The moisture flux on the material surface (fig.10) denoted j_{x^+} is obtained

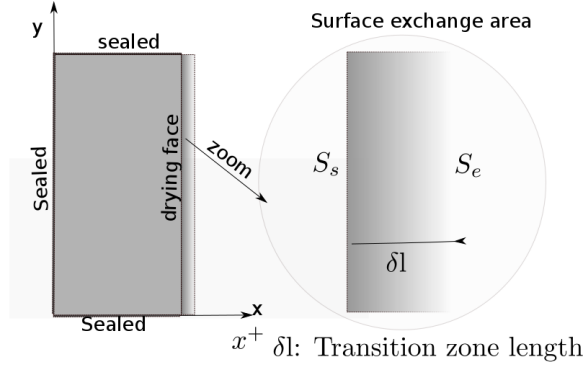


Figure 10: Sketching the boundary condition with surface effect

347 by projecting Eq.1 onto the normal direction x^+ and reads Eq.8:

$$j_{x^+} = D(S_l) \frac{\partial S_l}{\partial x} \quad (8)$$

348 When the flux of water j_{x^+} from the bulk, driven by diffusion within the
 349 porous medium, is fast enough (thin specimen or highly porous materials)
 350 to exceed the evaporation rate at the surface, controlled by the surrounding
 351 environmental factors such as air velocity, temperature, humidity [34, 35],
 352 a humidity gradient is created between the surface of porous medium and
 353 region of air outside its influence. A moisture flux, j_{x^-} of vapour is then
 354 established. j_{x^-} is driven by vapor diffusion in air and is modeled by using
 355 Fick's law [34, 35] expressed in Eq.9:

$$j_{x^-} = D_{vs} \frac{\partial C_v}{\partial x} \quad (9)$$

356 where D_{vs} is the diffusivity of vapour of the surface, and C_v is the vapour
 357 concentration of air.

358 By defining the water saturation in the air in analogy with material
 359 saturation S_l as $C_v = \rho_v S$, Eq.9 rewrites in form of Eq.10:

$$j_{x^-} = \rho_v D_{vs} \frac{\partial S}{\partial x} \quad (10)$$

360 where ρ_v is the density of vapor water. Note that ρ_v , and D_{vs} depend on
 361 environment factors such as air temperature and humidity, air velocity [34].

362 The term $\frac{\partial S}{\partial x}$ of Eq.10 is the most difficult to deal with in evaporation
 363 problems [34]. A first approximation is to assume a linear variation of it in

Table 7: Values of boundary layer thickness δ and surface exchange coefficient C_s given different velocity of the air outside the boundary layer, $l = 10^{-3}$ [m]

U (10^{-3} m/s)	δ (10^{-3} m)	C_s (10^{-9} kg.m ⁻² s ⁻¹)
1	12	1.3
2	9	1.8
4	6	2.6
8	4	3.6
16	3	5

364 the transition zone [40], which is expressed as:

$$\frac{\partial S}{\partial x} = \frac{S_{mat} - S_{env}}{\delta} \quad (11)$$

365 where S_{mat} is the vapor saturation of the surface of porous medium, S_{env}
366 the vapor saturation of air out of zone of influence of the solid surface, and
367 δ the length of the transition zone.

368 Introducing Eq.11 in Eq.10 yields:

$$j_{x-} = C_s(S_{mat} - S_{env}) \quad (12)$$

369 where C_s is the so-called surface factor or surface mass loss coefficient
370 [kg.m⁻²s⁻¹], explicitly defined by

$$C_s = \frac{\rho_v D_{vs}}{\delta} \quad (13)$$

371 C_s may be identified by inverse analysis [40] on mass loss or by analytical
372 calculation [39] :

$$\delta = \sqrt{\frac{\nu l}{U}} \quad (14)$$

373 where U [m/s] is the flow velocity outside the boundary layer; ν [m²/s]
374 the kinetic viscosity, and l [m] is the drying thickness, which is considered
375 as the characteristic length of drying material. By taking $D_{vs} = D_0 \phi^{a_{mq}}$
376 (Millington's semi-empirical model [59]), Eqs.13, 14 allow to perform analyt-
377 ical calculations. The results displayed in tab.7, demonstrates that increas-
378 ing the air velocity U , decreases the boundary layer thickness and increases
379 the surface exchange coefficient.

380 *5.3. Numerical study of the moisture transfer coefficient*

381 Thanks to the calibrated model of the previous section, simulations were
382 performed on specimens 1, 2, and 5 mm in thickness. Two types of bound-
383 ary conditions were tested for each simulation. In the case of Robin type
384 boundary conditions, the mass loss transfer coefficient C_s was varied from
385 $10^{-5} \text{ kg.m}^{-2}.\text{s}^{-1}$ to $10^{-10} \text{ kg.m}^{-2}.\text{s}^{-1}$ (very low value, far from Dirichlet
386 boundary conditions) to cover a wide range of environmental drying condi-
387 tions (air change rate, temperature, humidity).

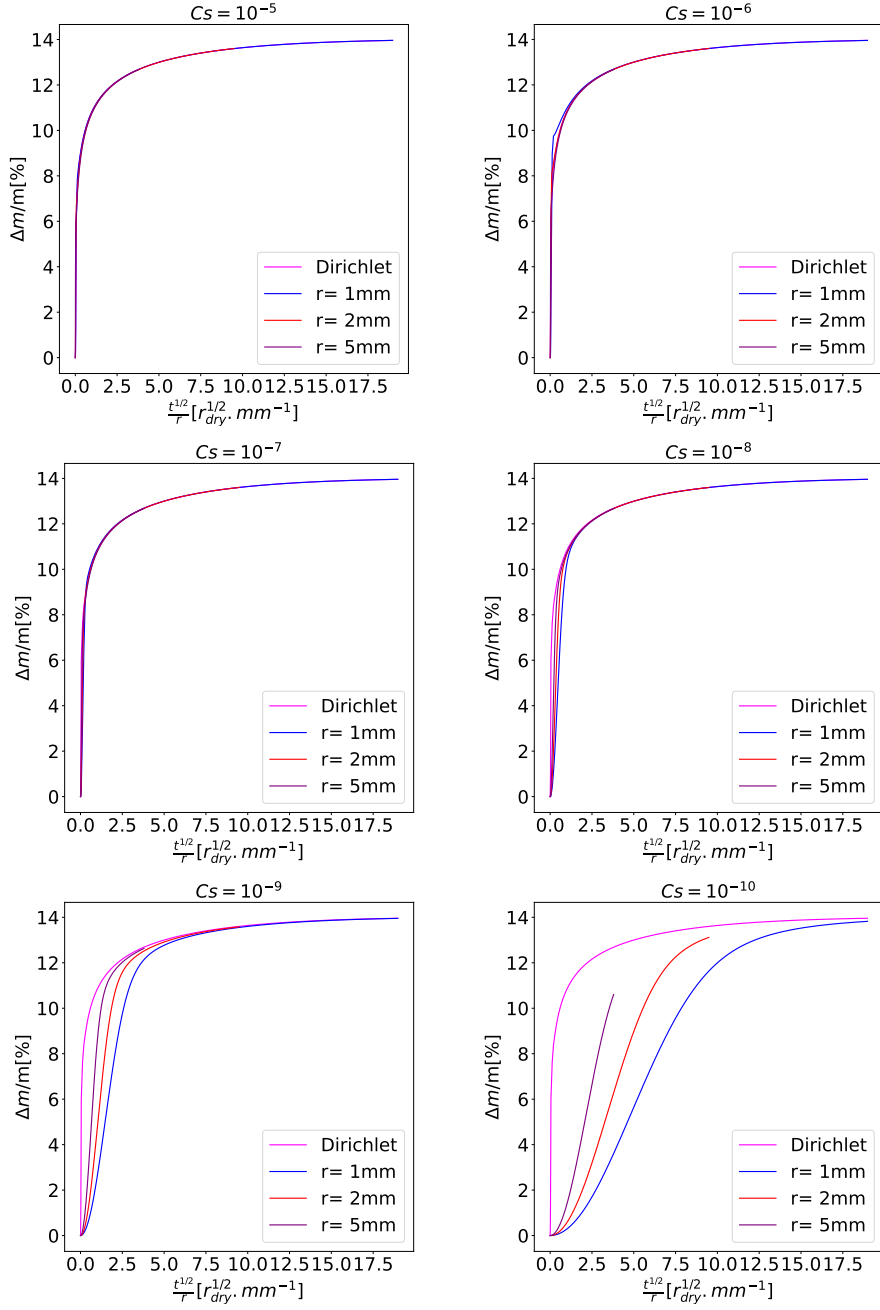


Figure 11: Evolution of mass loss, when using Dirichlet and Robin boundary conditions and different values of exchange coefficient C_s for specimens of different drying thickness r ; $\frac{t^{1/2}}{r}$ is the drying equivalent time.

388 According to the results of the sensitivity analysis shown in fig.11 for
389 mass loss, an exchange coefficient greater herein or equal to 10^{-7} gives iden-
390 tical results as Dirichlet condition, regardless of the specimen size. Those
391 results demonstrate that a threshold value of exchange coefficient exists
392 above which, whenever applying Dirichlet or Neumann type boundary con-
393 dition gives the same mass loss results independently of the specimen size.
394 In the numerical simulations undertaken, this value is found to be 10^{-7}
395 $kg.m^{-2}.s^{-1}$.

396 5.4. *Surface bulk constant number*

397 The sensitivity of the kinetics of mass loss is studied. The results dis-
398 played in fig.12 demonstrate that a threshold value exists above which the
399 kinetic of mass loss is the same regardless of the drying thickness or the ma-
400 terial intrinsic permeability. The threshold of exchange coefficient, which
401 separates convection to diffusion action on material surface is estimated to
402 be $10^{-7} kg.m^{-2}.s^{-1}$.

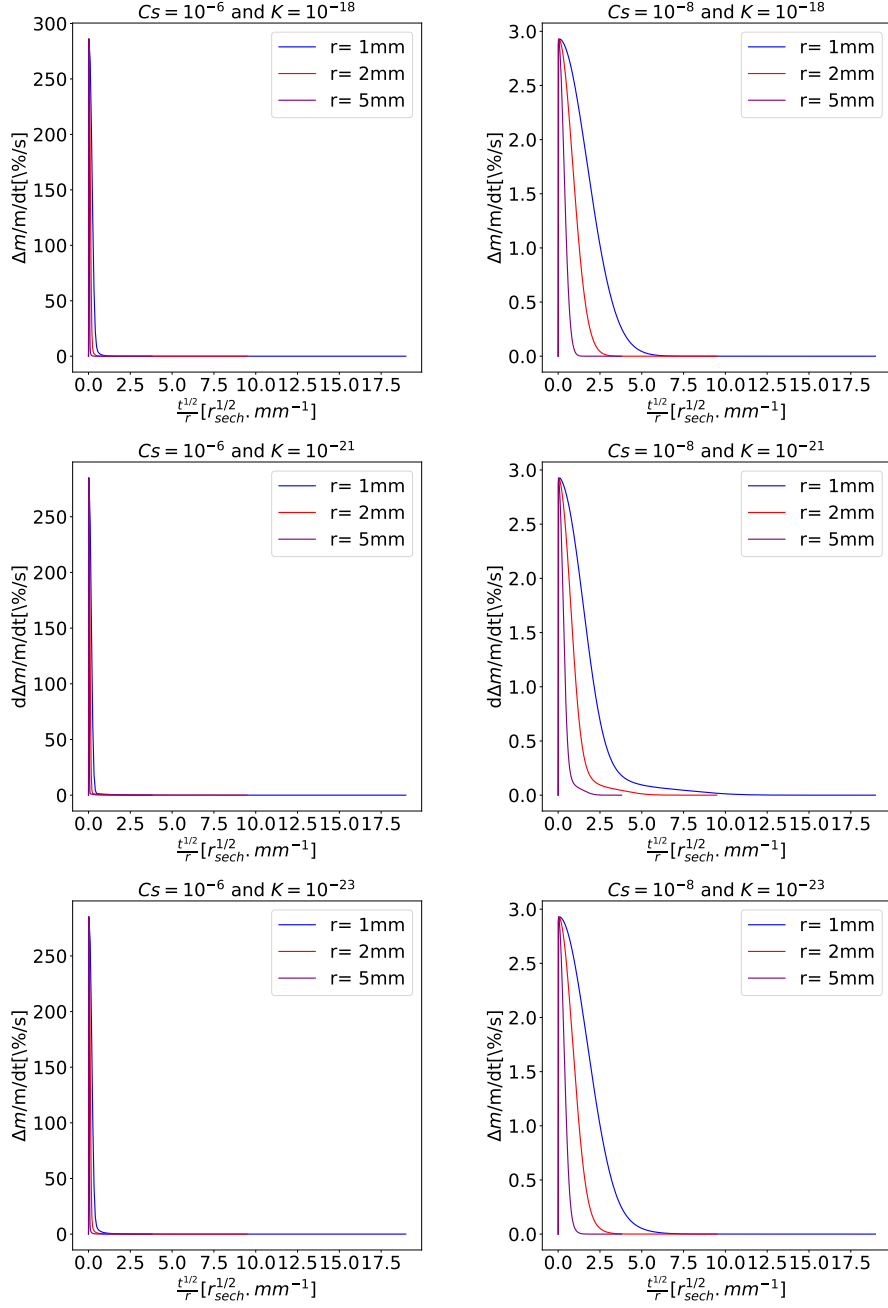


Figure 12: Kinetic of mass loss evolution for material intrinsic permeability of $K = 10^{-18}$, 10^{-21} and $10^{-23} m^2$, each for exchange coefficient $C_s = 10^{-6}$, 10^{-7} , $10^{-8} kg.m^{-2}.s^{-1}$ and drying thicknesses $r = 1, 2, 5 mm$

403 These results suggest that it is possible to derive a practical number,
 404 which will tell us whenever we are in or out of the zone of influence of the
 405 exchange coefficient (fig.10) for a given material (diffusivity D , dry material
 406 density ρ_d) of a given size (drying thickness l) exposed to certain drying
 407 condition (exchange coefficient C_s).

408 Considering a volume of water per unit area flowing along a drying
 409 thickness l and crossing surface A , the rate of evaporation noted R , is given
 410 by

$$R = -\frac{1}{A} \frac{dm}{dt} \quad (15)$$

411 Let us introduce the following dimensionless variables:

412 • $\vartheta = \frac{D_{sat}}{l^2} \times t$ the dimensionless time; where t [s] is the time, D_{sat}
 413 [$m^2.s^{-1}$] the average diffusivity of the material in a steady state; $l = \frac{V}{A}$,
 414 where $V[m^3]$ is the volume of the drying specimen and A its surface
 415 exposed to drying.

416 • $w = \frac{m}{m_f}$ the unit mass per dry material (mass at given time during
 417 drying normalized by the mass of completely dried material); $m =$
 418 $\rho_d \times A \times l \times w$, $m_f = \rho_d \times A \times l$. m_f is the mass of dry material and
 419 ρ_d the dry mass per unit volume.

420 Using these variables, Eq.15 becomes:

$$R = -\frac{\rho_d D_{sat}}{l} \frac{dw}{d\vartheta} \quad (16)$$

421 The continuity of moisture transfer rate on the surface requires that
 422 $R = j_x-$

$$R = -\frac{\rho_d D_{sat}}{l} \frac{dw}{d\vartheta} = C_s(S_s - S_e) \quad (17)$$

423 The left board side of Eq.17 is controlled by the diffusion process in
 424 bulk, while the right board side is a signature of the surface evaporation
 425 process. Therefore, we introduce the dimensionless Surface Bulk Constant
 426 SBC number.

$$SBC = \frac{C_s l}{\rho_d \times D_{sat}} \quad (18)$$

427 where l is the drying thickness, which is considered as the characteristic
 428 length of drying; C_s the surface exchange coefficient given by Eq.13, is com-
 429 pletely determined by the drying condition; and D_{sat} the water diffusivity
 430 in bulk at a steady state in concrete.

431 By combining Eqs.13, 14 and 18, we obtain a more explicit equation of
 432 SBC:

$$SBC = \frac{\rho_v}{\rho_d} \times \frac{D_{vs}}{D_{sat}} \times R_e^{1/2} \quad (19)$$

433 where $R_e = \frac{Ul}{\nu}$ is the Reynolds number which must satisfy $R_e < 1000$
 434 (laminar flow conditions). By analogy to the Biot number [78, 61], which
 435 expresses the ratio of the heat transfer resistance inside of a body to the
 436 heat transfer resistance of its surface, the SBC compares diffusion rate in
 437 bulk to that at the surface. It is noteworthy that by increasing drying thick-
 438 ness l , or air velocity U , or decreasing diffusivity D_{sat} , kinetic viscosity of
 439 air ν , the SBC number increases also, and the diffusion in the bulk con-
 440 crete dominates. Conversely, the smaller the specimen, the smaller SBC ,
 441 meaning that the surface effects become more and more dominant.

442 6. Experimental study and numerical modelling of drying shrink- 443 age

444 6.1. Mechanisms

445 Shrinkage of cement-based materials occurs over a broad range of scales
 446 from nanometer to the meter level. Four mechanisms are proposed to ex-
 447 plain drying shrinkage in the literature, and they all take place at the
 448 nanometer level. The mechanisms are well-documented thanks to inten-
 449 sive research since the pioneering work of [28], and [62], and we recall the
 450 definition of each mechanism briefly:

- 451 • Capillary pressure: the capillary pressure acts on the water–air
 452 menisci in the partially empty pores, which induces anisotropic com-
 453 pressive stress causing the rigid solid skeleton to shrink [23, 65].
- 454 • Movement of interlayer water: the microstructure of C-S-H is a
 455 layered-bricks structure with water molecules in between. Therefore,
 456 the removal of water due to drying will cause C-S-H sheets to shrink,
 457 which results in macroscopic contractions [45].

- 458 • Surface tension: a molecule of water within the material is under
459 attractive and repulsive forces in all directions from neighbouring
460 molecules. But in the case of molecules lying on the surface, due
461 to lack of symmetry, there is a non-zero resultant force perpendicular
462 to the surface, causing its contraction like a stretched elastic skin [27].
- 463 • Disjoining pressure: it is visualized as the force pushing apart adjacent
464 solid particles on water penetration in regions where free adsorption
465 related to Van der Waals forces cannot fully develop when relative
466 humidity is increased. As a direct consequence of drying, the removal
467 of this interlayer water will cause the disjoining pressure to decrease
468 and the particles to shrink [53].

469 6.2. Drying shrinkage model

470 These driving mechanisms of drying shrinkage of cement-based materials
471 are still frequently debated in the literature. During the past years, several
472 shrinkage models have been proposed for drying shrinkage of cement-based
473 materials [23, 6, 73, 82, 66, 4, 27, 3]. In the framework of poroelasticity,
474 [23] modeled the macroscopic shrinkage by considering both capillary stress
475 and surface tension effects (Eq.21).

$$\dot{\epsilon}_{sh} = \frac{bS_l}{K_b} \dot{P}_c \quad (20)$$

476 where b is the Biot coefficient written as $b = 1 - \frac{K_b}{K}$; K stands for the bulk
477 modulus of the matrix, K_b stands for the bulk modulus of the skeleton (dry
478 material); S_l the water degree of saturation; P_c the capillary pressure is
479 ruled by Kelvin law:

$$\dot{\epsilon}_{sh} = \frac{bS_l}{K_b} \dot{P}_c \quad (21)$$

480 where b is the Biot coefficient written as $b = 1 - \frac{K_b}{K}$; K stands for the
481 bulk modulus of the matrix, K_b stands for the bulk modulus of the skeleton
482 (dry material); S_l the water degree of saturation; P_c the capillary pressure
483 is ruled by Kelvin law:

$$P_c = \rho_l \frac{RT}{M} \ln(RH) \quad (22)$$

484 In Eq.22, ρ_l [kg/m^3] is the density of liquid, M the molar mass of the water
485 vapor [kg/mol], $R=8.314$ [$J/(mol.K)$] the universal gas constant, T [K] the

486 temperature. Combining Eqs.21,22 reads Eq.23 known as Coussy model
 487 [23] that accounts for both capillary stress and surface effects:

$$\dot{\epsilon}_{sh} = \frac{bS_l}{K_b} \rho_l \frac{RT}{M} \frac{\dot{h}}{h} \quad (23)$$

488 In this study we considered the model of Eq.24,

$$\dot{\epsilon}_{sh} = k_{sh} \frac{\dot{h}}{h} \quad (24)$$

489 where k_{sh} [-] is the shrinkage coefficient, h is the relative humidity. This
 490 model corroborates with experimental observations performed on thin ce-
 491 ment paste samples in order to get rid of cracking [25, 6, 53, 50], especially
 492 for relative humidity range above 40-50% RH. The measure is then an in-
 493 trinsic response of the material, and the single parameter of the constitutive
 494 law corresponds to the experimental curve slope. The purpose of this sec-
 495 tion is to stress out this model regarding its capability to perform well for
 496 different scales and for relative humidity down to 20% RH. In the following,
 497 the model parameter is calibrated from experimental measurements, and
 498 the ability of the model to predict drying shrinkage from micrometer-scale
 499 to centimeter-scale is tested. The drying strain is analyzed, assuming that
 500 endogenous shrinkage can be neglected since all the specimens involved in
 501 this study were well hydrated. They are at least three months old, and the
 502 water to cement ratio was sufficiently large.

503 6.3. Experimental determination of drying shrinkage coefficient

504 In a first attempt, the drying shrinkage coefficient is assessed experimen-
 505 tally thanks to experiment P500 μ m-CC-LCIs. The coefficient of shrinkage
 506 is considered to be the ratio between the shrinkage over the relative humid-
 507 ity difference. The value of this coefficient is found to be $k_{sh} = 8.6 \times 10^{-5}$
 508 for the experimental result displayed in fig.13. The duration for equilibrium
 509 at different relative humidity steps is reported in tab.8.

Table 8: Duration for equilibrium at different relative humidity steps

Relative humidity (%)	80	60	42	27	20
Duration (h)	24	24	30	60	165

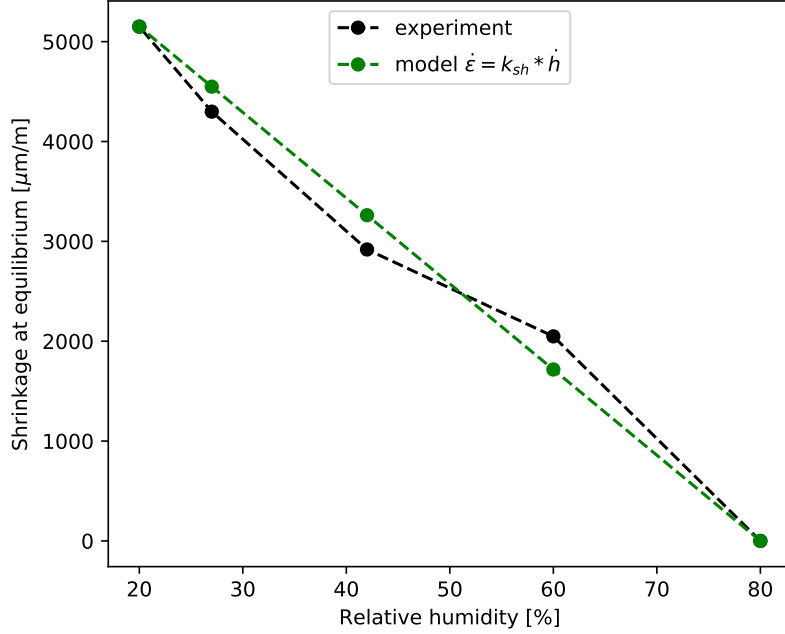


Figure 13: Determination of drying shrinkage coefficient $k_{sh} = 8.6 \times 10^{-5}$ by sorption length change measurements on a small prism (experiment P500 μ m-CC-LCIs), performed in climatic chamber.

510 *6.4. Prediction of drying shrinkage*

511 Specimen of various sizes are used for different drying kinetics, and
 512 strains are measured at different scales. Using the identified drying shrink-
 513 age coefficient $k_{sh} = 8.6 \times 10^{-5}$ [-] to perform finite element simulations,
 514 the experimental results of drying shrinkage from centimeter to micrometer
 515 scales are well reproduced. centimeter scale is shown on fig.14, millimeter
 516 scale on fig.15 and micrometer scale on fig.16 and fig.17.

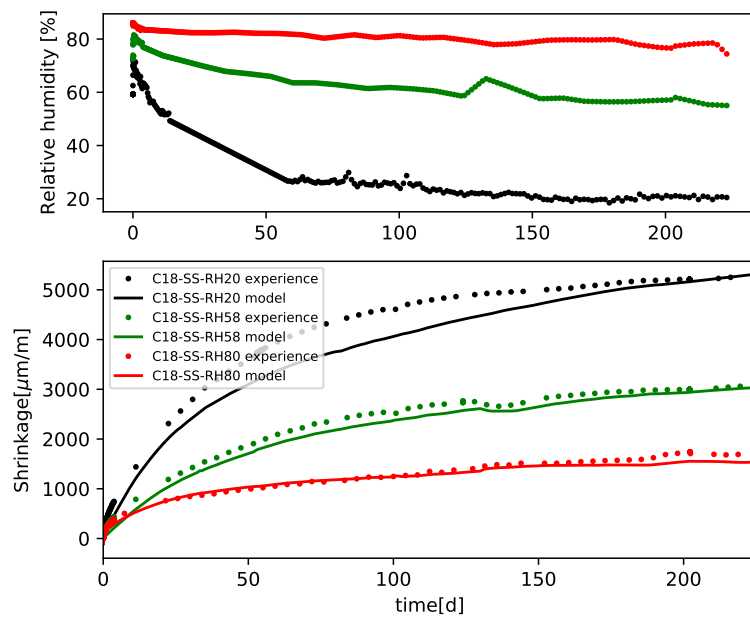


Figure 14: Prediction of drying shrinkage at centimeter level using $k_{sh}\dot{h}$ model, with the parameters identified above for experiments C18-SS-RH80, C18-SS-RH58 and C18-SS-RH20

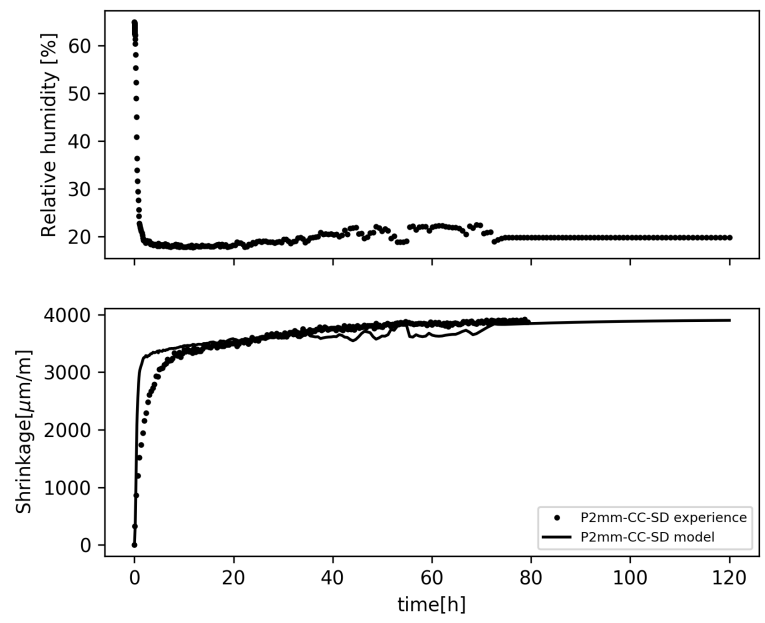


Figure 15: Prediction of drying shrinkage of small prism P2mm-CC-SD with 1 mm drying thickness using the parameters identified above.

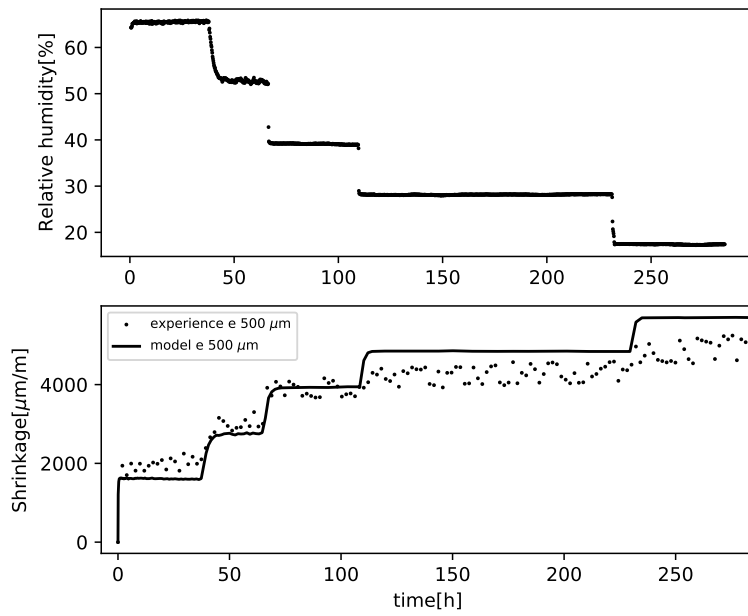


Figure 16: Prediction of drying shrinkage of small prism P500 μm -CC-LCIs with 0.25 mm drying thickness using the parameters identified above.

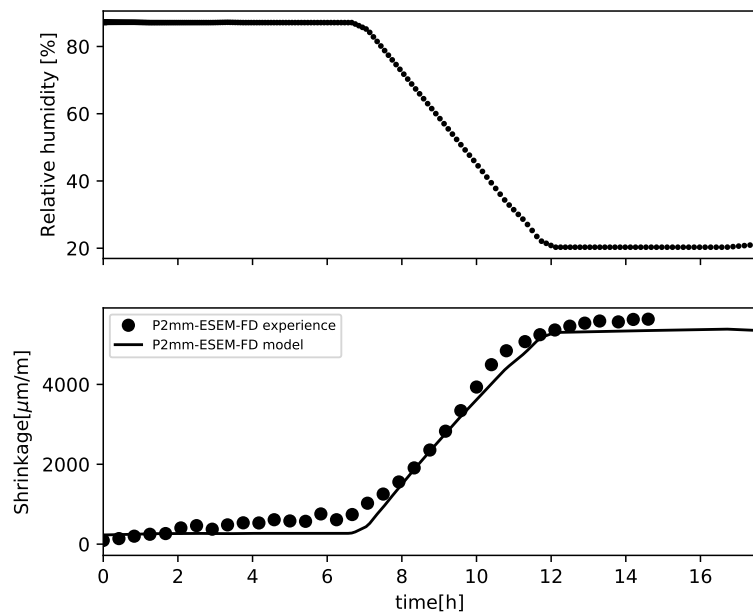


Figure 17: Prediction of drying shrinkage of small prism P2mm-ESEM-FD with 1 mm drying thickness using the parameters identified above.

517 For each case, a drying simulation was performed first using the dry-
518 ing model identified in the previous section (the parameters were kept the
519 same), and the result was used to feed the mechanical calculations. This
520 suggests that the drying model identification is trustworthy. The agreement
521 with experimental results also tells us that, for the cement paste, if the water
522 desorption isotherm of material is measured, and if drying of the material
523 can be simulated, the drying shrinkage can be predicted in a straightfor-
524 ward manner. A single experiment of a few days duration helps to identify
525 the drying shrinkage coefficient. Considering the pore relative humidity as
526 a primary variable for shrinkage and saturation for drying is a good com-
527 bination for the prediction of drying shrinkage. Yet, the simulations were
528 performed only on cement paste specimens in this study, and a similar work
529 should be performed on concrete, with the combination of homogenizations
530 calculations.

531 *6.5. Analysis of internal stresses profiles*

532 By post-processing the drying shrinkage simulations results, we obtain
533 the self-equilibrated stresses across the specimen thickness, fig.18. Self-
534 equilibrated stresses develop for two main reasons: (i) macroscopic non-
535 uniformity of the drying process, and if the local stress induced by hydric
536 gradient exceeds the tensile strength of the material, micro-cracking will
537 occur; (ii) the second origin of local stresses is due to the incompatibility
538 of shrinking phases (mainly C-S-H) and non-shrinking phases (CH, for in-
539 stance) of the material. Similarly, if the self-restraint stress exceeds the ten-
540 sile strength, micro-cracking occurs. Fig.18 shows self-equilibrated stresses,
541 resulting from the combination of these phenomena.

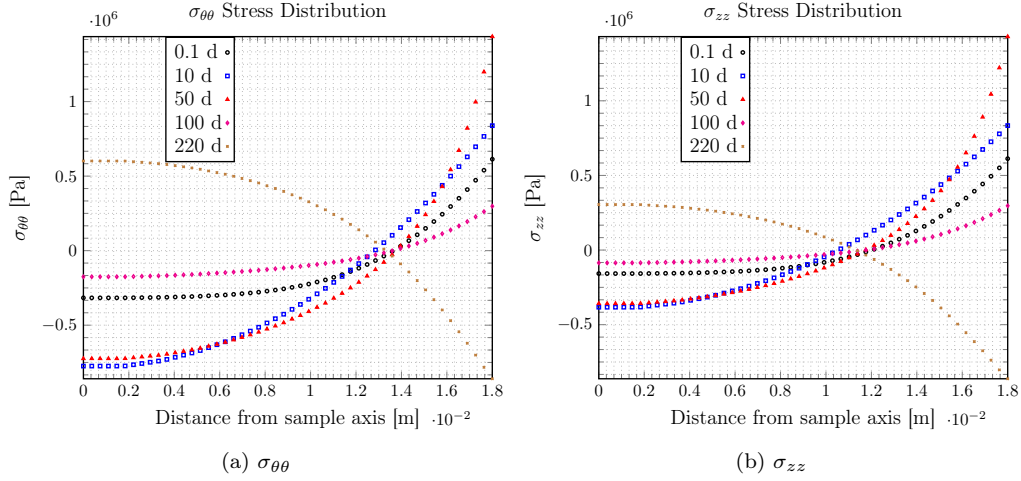


Figure 18: Stress Distribution along the central radius of cylindrical $\phi 36 \times 180$ mm specimen submitted to environmental variable relative humidity (ref fig.9.b)-C18mm-RH60)

542 During the first stage of drying, the specimen surface experiences ten-
543 sile stresses, while the core is under compressive stresses. The tensile stress
544 grows to reach a maximum of 1.5 MPa after about 50 days of drying and
545 then decreases. At the final drying stage, the stress profile is inverted, the
546 core is under tension while the surface is under compression. It is notewor-
547 thy to highlight that, despite the relatively large dimensions of $\phi 36 \times 180$
548 mm cylinders (equivalent drying thickness of 18 mm), drying has not in-
549 duced micro-cracking since the stress gradients reported in fig.18 remains
550 under the tensile strength of the material ($f_t \approx 2.5 - 3$ MPa). This is also
551 supported by the analysis of water profiles displayed in fig.9. The develop-
552 ment of internal stress due to drying is limited because the prescribed drying
553 humidity was slow enough; therefore the skin-micro-cracking due to to limit
554 the rise of hydric gradient stress is avoided, and the measured shrinkage can
555 be considered as uniform within the specimen at this investigation scale.

556 7. Conclusion

557 Drying and drying shrinkage experiments were performed on cement
558 paste using different geometries: cylinder $\phi 36$ mm in diameter and thin
559 prisms of 0.5, 1, 2 mm thick. The specimens were dried at various rates and
560 with different steps of humidity, using different conditioning systems: envi-
561 ronmental scanning electronic microscope (ESEM), climatic chamber (CC),

562 Dynamic Vapor Sorption (DVS), and saturated salt solution (SSS). Drying
563 modelling was performed via a Richards-Fick model, which accounts for
564 water permeation and vapour diffusion. Moisture transport properties were
565 back-calculated by inverse FE analysis on mass loss. A sensitivity study is
566 proposed to determine which type of boundary conditions is the most suit-
567 able for drying analysis. Drying shrinkage as the mechanical consequence
568 of drying is also analyzed. The following conclusions can be drawn:

- 569 • The drying model account well for size effects, which is crucial for the
570 practical transposition of such model from the laboratory scale to the
571 structural scale.
- 572 • The effect of surface exchange coefficient on the moisture profiles is
573 very significant, specifically near the drying surface. And the resulting
574 stress-gradients are reduced.
- 575 • The sensitivity analysis of surface exchange shows that it is unnec-
576 essary to use mixed boundary conditions when the diffusion in the
577 material is slower than the diffusion in the air.
- 578 • The surface bulk constant (SBC) concept shows how different factors,
579 including environmental conditions, specimen geometry and material
580 properties, affect the surface evaporation of cement-based materials.
581 We propose an analytical formula for determining the surface exchange
582 coefficient.
- 583 • Drying shrinkage bears a quasi-linear relationship with relative humid-
584 ity. The drying shrinkage model $\dot{\epsilon} = k_h \frac{\dot{h}}{h}$ is found to be trustworthy for
585 a broad range of humidities ranging from 95% to 20 %. The coefficient
586 of proportionality is independent of the size and drying rate.

587 As a perspective, we could think of predicting drying shrinkage at the con-
588 crete scale and further on the structural scale with this model type based on
589 single length change measurement. The linearity of drying shrinkage with
590 relative humidity makes it possible to fully calibrate the model for large rel-
591 ative humidity ranges based on one single drying shrinkage experiment. It
592 will be time effective to carry out experiments on cement paste and retrieve
593 the corresponding coefficient for concrete through homogenization.

594 **Acknowledgments**

595 This study was funded by EDF R&D and Association Nationale de
596 Recherche et de Technologie (ANRT), and Laboratoire de Mecanique et
597 de Technologie (LMT). The authors wish to thank all the contributors to
598 this study: Alexis Legrix, Didier Leroy, Michel Mahe, Nicolas Brynaert are
599 gratefully thanked for their assistance in experiments' design and realiza-
600 tion.

601 **References**

- 602 [1] P. Acker and F-J. Ulm. Creep and shrinkage of concrete: physical origins and
603 practical measurements. *Nuclear Engineering and Design*, 203(2):143–158, 2001.
- 604 [2] J-L. Adia, Charpin L., B. Martin, D. Leroy, B. Masson, and A. Courtois. In-situ rh
605 measurements in concrete in a variable temperature environment.
- 606 [3] J-L. Adia, J. Yvonnet, Q-C. He, N.C. Tran, and J. Sanahuja. A combined lattice-
607 boltzmann-finite element approach to modeling unsaturated poroelastic behavior of
608 heterogeneous media. *Journal of Computational Physics*, 437:110334, 2021.
- 609 [4] J-L. D. Adia, J. Yvonnet, Q-C. He, N-C. Tran, and J. Sanahuja. Elastic shrinkage-
610 swelling modeling in porous microstructures: a combined finite elements-lattice
611 boltzmann-numerical approach. In *Poromechanics VI*, pages 378–385. 2017.
- 612 [5] V. Baroghel-Bouny. Water vapour sorption experiments on hardened cementitious
613 materials. Part I: Essential tool for analysis of hygral behaviour and its relation to
614 pore structure. *Cement and Concrete Research*, 2007.
- 615 [6] V. Baroghel-Bouny, M Mainguy, T Lassabatere, and Olivier Coussy. Characteriza-
616 tion and identification of equilibrium and transfer moisture properties for ordinary
617 and high-performance cementitious materials. *Cement and concrete research*, 29(8):
618 1225–1238, 1999.
- 619 [7] Z.P. Bazant and J C Chern. Concrete creep at variable humidity: constitutive law
620 and mechanism. *Materials and structures*, 18(1):1, 1985.
- 621 [8] Z.P. Bažant and M Jirásek. *Creep and hygrothermal effects in Concrete Structures*.
622 Springer New York LLC, 2018.
- 623 [9] Z.P. Bazant and F.H. Wittmann. Creep and shrinkage in concrete structures. 1982.
- 624 [10] Z.P. Bažant, A A Asghari, and J Schmidt. Experimental study of creep of hardened
625 Portland cement paste at variable water content. *Materials and Structures*, 9(4):
626 279–290, 1976.
- 627 [11] F. Benboudjema and J-M Torrenti. Prediction of mechanical consequences of drying:
628 From laboratory to concrete structures. *Cement and concrete research*, 42(7):1014–
629 1023, 2012.
- 630 [12] F. Benboudjema, F. Meftah, and J-M. Torrenti. Interaction between drying, shrink-
631 age, creep and cracking phenomena in concrete. *Engineering structures*, 27(2):239–
632 250, 2005.
- 633 [13] F. Bendboudjema. *Modélisation des déformations différées du béton sous sollicita-
634 tions biaxiales. Application aux confinements des réacteurs des centrales nucléaires*.
635 PhD thesis, Université de Marne la Vallée, 2002.
- 636 [14] J. Bisschop and F.K. Wittel. Contraction gradient induced microcracking in hard-
637 ened cement paste. *Cement and Concrete Composites*, 33(4):466–473, 2011.
- 638 [15] B. Bissonnette, P. Pierre, and M. Pigeon. Influence of key parameters on drying
639 shrinkage of cementitious materials. *Cement and Concrete Research*, 29(10):1655–
640 1662, 1999.
- 641 [16] N. Burlion, F. Bourgeois, and J-F. Shao. Effects of desiccation on mechanical be-
642 haviour of concrete. *Cement and concrete composites*, 27(3):367–379, 2005.
- 643 [17] H. Cagnon, T. Vidal, A. Sellier, X. Bourbon, and G. Camps. Cement and Concrete
644 Research Drying creep in cyclic humidity conditions. *Cement and Concrete
645 Research*, 76:91–97, 2015. ISSN 0008-8846. doi: 10.1016/j.cemconres.2015.05.015.
- 646 [18] L. Charpin, A. Courtois, F. Taillade, B Martin, B. Masson, and J. Haelewyn. Cali-

- 647 bration of Mensi/Granger constitutive law: evidences of ill-posedness and practical
648 application to VeRCoRs concrete. In *SMSS*, 2018.
- 649 [19] L. Charpin, Y. Le Pape, E. Coustabeau, E. Toppani, G. Heinfling, C. Le Bellego,
650 B. Masson, J. Montalvo, A. Courtois, J. Sanahuja, and N. Reviron. A 12 Year EDF
651 Study of Concrete Creep under Uniaxial and Biaxial Loading. *Cement and Concrete*
652 *Research*, 103:140–159, 2018. doi: 10.1016/j.cemconres.2017.10.009.
- 653 [20] L. Charpin, J. Niepceron, M. Corbin, B. Masson, J-P. Mathieu, J. Haelewyn, F. Ha-
654 mon, M. Àhs, S. Aparicio, and M. and others Asali. Ageing and air leakage assess-
655 ment of a nuclear reactor containment mock-up: Vercors 2nd benchmark. *Nuclear*
656 *Engineering and Design*, 377:111136, 2021.
- 657 [21] Y. Chen, J. Wei, H. Huang, W. Jin, and Q. Yu. Application of 3d-dic to characterize
658 the effect of aggregate size and volume on non-uniform shrinkage strain distribution
659 in concrete. *Cement and Concrete Composites*, 86:178–189, 2018.
- 660 [22] A. Courtois, F. Taillade, and D. Placko. Some considerations on the benefit of mea-
661 suring concrete moisture to predict long term structural behaviour. *Construction*
662 *and Building Materials*, 265:120283, 2020.
- 663 [23] O. Coussy, P. Dangla, T. Lassabatere, and V. Baroghel-Bouny. The equivalent pore
664 pressure and the swelling and shrinkage of cement-based materials. *Materials and*
665 *structures*, 37:15–20, 2004.
- 666 [24] J. Crank. *The Mathematics of Diffusion*. OXFORD UNIVERSITY PRESS, 2002.
667 ISBN 0 19 853344 6.
- 668 [25] R L Day, P Cuffaro, and J M Illston. The effect of rate of drying on the drying creep
669 of hardened cement paste. *Cement and Concrete Research*, 14(3):329–338, 1984.
- 670 [26] A. Djerbi, S. Bonnet, A. Khelidj, and V. Baroghel-Bouny. Influence of traversing
671 crack on chloride diffusion into concrete. *Cement and Concrete Research*, 38(6):
672 877–883, 2008.
- 673 [27] G. El Tabbal, P. Dangla, M. Vandamme, M. Bottoni, and S. Granet. Modelling the
674 drying shrinkage of porous materials by considering both capillary and adsorption
675 effects. *Journal of the Mechanics and Physics of Solids*, page 104016, 2020. ISSN
676 0022-5096. doi: <https://doi.org/10.1016/j.jmps.2020.104016>.
- 677 [28] R. F. Feldman and P. J. Sereda. Sorption of water on compacts of bottle-hydrated
678 cement. i. the sorption and length-change isotherms. *Journal of Applied Chemistry*,
679 1964.
- 680 [29] A. Foucault, S. Michel-Ponnelle, and E. Galenne. A new creep model for NPP
681 containment behavior prediction. In *Proceedings of the 1st SSCS (Strategies for*
682 *Sustainable Concrete Strategies)*, 2012.
- 683 [30] H. Garbalinska, M. Bochenek, W. Malorny, and J. Von Werder. Comparative anal-
684 ysis of the dynamic vapor sorption (dvs) technique and traditional method for
685 sorption isotherms determination-exemplified at autoclaved aerated concrete sam-
686 ples of four density classes. *Cement and Concrete Research*, 91:97–105, 2017.
- 687 [31] L Granger. *Comportement difféé du béton dans les enceintes de centrales nucléaires:*
688 *analyse et modélisation*. PhD thesis, Ecole Nationale des ponts et Chaussées, 1995.
- 689 [32] Z.C. Grasley, D.A. Lange, and D.D. Matthew. Internal relative humidity and drying
690 stress gradients in concrete. *Materials and Structures*, 39(9):901–909, 2006.
- 691 [33] V. Guihard, C. Patapy, J. Sanahuja, J. Balayssac, F. Taillade, and B. Steck. Ef-
692 fective medium theories in electromagnetism for the prediction of water content in

- 693 cement pastes. *International Journal of Engineering Science*, 150:103273, 2020.
- 694 [34] C. Hall and W.D. Hoff. *Water transport in brick, stone and concrete*. CRC Press,
695 2002.
- 696 [35] M.R. Hall and D. Allison. Evaporative drying in stabilised compressed earth mate-
697 rials using unsaturated flow theory. *Building and Environment*, 45:509–518, 2010.
- 698 [36] W. Hansen. Drying Shrinkage Mechanisms in Portland Cement Paste. *Journal*
699 *of the American Ceramics Society*, 70(5):323–328, 1987. ISSN 1551-2916. doi:
700 10.1111/j.1151-2916.1987.tb05002.x.
- 701 [37] A. Hilaire. *Etude des déformations différées des bétons en compression et en trac-*
702 *tion, du jeune au long terme: application aux enceintes de confinement*. PhD thesis,
703 Ecole normale supérieure Cachan, 2014.
- 704 [38] F. Hild and S. Roux. CORRELI Q4 : A Software for "Finite-element" Displacement
705 Field Measurements by Digital Image Correlation Internal report no. 269. Technical
706 report, LMT, France, 2008.
- 707 [39] K. Hisatake, M. Fukuda, J. Kimura, M. Maeda, and Y. Fukuda. Experimental and
708 theoretical study of evaporation of water in a vessel. *Journal of applied physics*, 77
709 (12):6664–6674, 1995.
- 710 [40] Q. Huang, Z. Jiang, X. Gu, W. Zhang, and B. Guo. Numerical simulation of
711 moisture transport in concrete based on a pore size distribution model. *Journal of*
712 *engineering mechanics*, 67:31–43, 2015.
- 713 [41] S. Huang. *Ageing behaviour of concrete creep : application to the VeRCoRs concrete*.
714 PhD thesis, Université Paris-Est, 2018.
- 715 [42] C-L. Hwang and J.F. Young. Drying shrinkage of portland cement pastes i. micro-
716 cracking during drying. *Cement and Concrete Research*, 14(4):585–594, 1984.
- 717 [43] A. Idiart, J. Bisschop, A. Caballero, and P. Lura. A numerical and experimental
718 study of aggregate-induced shrinkage cracking in cementitious composites. *Cement*
719 *and Concrete Research*, 42(2):272–281, 2012.
- 720 [44] T. Ishida and W. Tiao. Future of multiscale modelling of concrete-Toward a full in-
721 tegration of cement chemistry and concrete structural engineering. *Rilem Technical*
722 *Letters*, 2018. doi: 10.21809/rilemtechlett.2018.60.
- 723 [45] H.M. Jennings. Refinements to colloid model of C-S-H in cement: CM-II. *Cement*
724 *and Concrete Research*, pages 275–289, 2008.
- 725 [46] M. Jirásek and P. Havlásek. Microprestress–solidification theory of concrete creep:
726 Reformulation and improvement. *Cement and Concrete Research*, 60:51–62, 2014.
- 727 [47] V. Kanna, R.A. Olson, and H.M. Jennings. Effect of shrinkage and moisture content
728 on the physical characteristics of blended cement mortars. *Cement and Concrete*
729 *Research*, 28(10):1467–1477, 1998.
- 730 [48] Emmanuel Keita. *Physique du séchage des sols et des matériaux de construction*.
731 PhD thesis, Paris Est, 2014.
- 732 [49] J. Kinda, L. Charpin, J-L. Adia, F. Benboudjema, and S. Michel-Ponnelle. Impact
733 of drying rate on delayed strains in cement-based materials. In *Interdisciplinary*
734 *Approaches for Cement-based MAterials and Structural Concrete: Synergizing Ex-*
735 *pertise and Bridging Scales of Space and Time*, pages 719–723, 2018.
- 736 [50] J. Kinda, A. Bourdot, L. Charpin, S. Michel-Ponnelle, and F. Benboudjema. In-
737 vestigation of drying shrinkage of cement based materials assisted by digital image
738 correlation. *Journal of Materials in Civil Engineering*, 2021.

- 739 [51] M. Mainguy. *Modèles de diffusion non linéaire en milieux poreux. Applications a la*
740 *dissolution et au séchage des matériaux cimentaires*. PhD thesis, ENPC - École des
741 Ponts ParisTech, 1999.
- 742 [52] M. Mainguy, O. Coussy, and V. Baroghel-Bouny. Role of air pressure in drying of
743 weakly permeable materials. *Journal of engineering mechanics*, 127:582–592, 2001.
- 744 [53] I. Maruyama. Origin of Drying Shrinkage of Hardened Cement Paste: Hydration
745 Pressure. *Journal of Advanced Concrete Technology*, 2010. ISSN 1346-8014. doi:
746 10.3151/jact.8.187.
- 747 [54] I. Maruyama. Multi-scale review for possible mechanisms of natural frequency
748 change of reinforced concrete structures under an ordinary drying condition. *Journal*
749 *of Advanced Concrete Technology*, 14(11):691–705, 2016.
- 750 [55] I. Maruyama, Y. Nishioka, G. Igarashi, and K. Matsui. Microstructural and bulk
751 property changes in hardened cement paste during the first drying process. *Cement*
752 *and Concrete Research*, 2014. ISSN 00088846. doi: 10.1016/j.cemconres.2014.01.007.
- 753 [56] J.P. Mathieu, L. Charpin, P. Sémété, C. Toulemonde, G.H.J. Boulant, and F. Tail-
754 lade. Temperature and humidity-driven ageing of the VeRCoRs mock-up. In *Computa-*
755 *tional7 Modelling of Concrete Structures*. In *Computational Modelling of Concrete*
756 *and Concrete Structures*, 2018.
- 757 [57] T. Mauroux, F. Benboudjema, P. Turcry, A. Aït-Mokhtar, and O. Deves. Study of
758 cracking due to drying in coating mortars by digital image correlation. *Cement and*
759 *Concrete Research*, 2012. ISSN 00088846. doi: 10.1016/j.cemconres.2012.04.002.
- 760 [58] B. Menu, M. Jolin, B Bissonnette, and L. Molez. Evaluation de la sensibilité à
761 la fissuration des bétons projetés au jeune âge. In *Proceedings of the Conférence*
762 *Internationale Francophone NoMaD 2018*, 2018.
- 763 [59] R.J. Millington. Gas diffusion in porous media. *Science*, 130(3367):100–102, 1959.
- 764 [60] Y. Mualem. A new model for predicting the hydraulic conductivity of unsaturated
765 porous media. *Water resources research*, 12(3):513–522, 1976.
- 766 [61] O. Omini, A. Sparavigna, and A. Strigazzi. Thermal diffusivity and biot num-
767 ber: A new experimental method. *Applied Physics*, 50:35–37, 1990. doi: 10.1007/
768 BF00323951.
- 769 [62] T.C. Powers. The thermodynamics of volume change and creep. *Matériaux et Con-*
770 *structon*, 6, 1968.
- 771 [63] S. Poyet, K. Trentin, and Amblard E. The use of sorption balance for the character-
772 ization of the water retention curve of cement-based materials. *Journal of Advanced*
773 *Concrete Technology*, 14:354–367, 2016.
- 774 [64] S. Rahimi-Aghdam, Z.P. Bažant, and G. Cusatis. Extended Microprestress-
775 Solidification Theory for Long-Term Creep with Diffusion Size Effect in Con-
776 crete at Variable Environment. *Journal of engineering mechanics*, 2019. doi:
777 10.1061/(ASCE)EM.1943-7889.0001559.
- 778 [65] T. Rougelot, F. Skoczylas, and N. Burlion. Water desorption and shrinkage in
779 mortars and cement pastes: Experimental study and poromechanical model. *Cement*
780 *and Concrete Research*, 2009. ISSN 00088846. doi: 10.1016/j.cemconres.2008.10.005.
- 781 [66] T. Rougelot, F. Skoczylas, and N. Burlion. Water desorption and shrinkage in
782 mortars and cement pastes: experimental study and poromechanical model. *Cement*
783 *and Concrete Research*, 39(1):36–44, 2009.
- 784 [67] C De Sa, F Benboudjema, M Thiery, and J Sicard. Cement & Concrete Compos-

- ites Analysis of microcracking induced by differential drying shrinkage. *Cement and Concrete Composites*, 30(10):947–956, 2008. ISSN 0958-9465. doi: 10.1016/j.cemconcomp.2008.06.015. URL <http://dx.doi.org/10.1016/j.cemconcomp.2008.06.015>.
- [68] Saba P., Honorio T., Mahmood O.-A., Benboudjema F. International rilem conference on early-age and long-term crack width analysis in rc structures. ENS Paris-Saclay, 2021.
- [69] H. Samouh, A. Soive, E. Rozière, and A. Loukili. Experimental and numerical study of size effect on long-term drying behavior of concrete: influence of drying depth. *Materials and Structures*, 49(10):4029–4048, 2016.
- [70] H. Samouh, E. Rozière, and A. Loukili. The differential drying shrinkage effect on the concrete surface damage: Experimental and numerical study. *Cement and Concrete Research*, 102:212–224, 2017.
- [71] H. Samouh, E. Rozière, and A. Loukili. Experimental and numerical study of the relative humidity effect on drying shrinkage and cracking of self-consolidating concrete. *Cement and Concrete Research*, 2019. ISSN 00088846. doi: 10.1016/j.cemconres.2018.08.008.
- [72] G.W. Scherer. Drying, shrinkage, and cracking of cementitious materials. *Transport in Porous Media*, 110(2):311–331, 2015.
- [73] B.A. Schrefler, L. Simoni, and C.E. Majorana. A general model for the mechanics of saturated-unsaturated porous materials. *Materials and Structures*, 22(5):323–334, 1989.
- [74] Mamadou Diaga Seck. *Compréhension des mécanismes de séchage dans les matériaux de construction: cas du plâtre*. PhD thesis, Paris Est, 2015.
- [75] A. Sellier, S. Multon, L. Buffo-Lacarrière, T. Vidal, Bourbon X., and G. Camps. Concrete creep modelling for structural applications: non-linearity, multi-axiality, hydration, temperature and drying effects. *Cement and concrete research*, 2016. doi: 10.1016/j.cemconres.2015.10.001.
- [76] C. Simon, F. G. Fernandez, L. G Esteban, P. Palacios, R. Hosseinpourpia, and C. Mai. Comparison of the saturated salt and dynamic vapor sorption method in obtaining the sorption properties of pinus pinea l. *European journal of Wood and Wood Products*, 75(6):919–926, 2017.
- [77] H.C. Sleiman, M. Briffaut, Dal Pont S., A. Tengattini, and B. Huet. Influence of common simplifications on the drying of cement-based materials up to moderate temperatures. *International Journal of Heat and Mass Transfer*, 150, 2020.
- [78] P. G. Smith. *Thermal processing of food*. Springer, 2011. ISBN 978-1-4419-7661-1. doi: 10.1007/978-1-4419-7662-8.
- [79] F. Soleilhet. *Etudes expérimentales et numériques des matériaux cimentaires sous sollicitations hydro-mécaniques*. PhD thesis, Cachan, Ecole normale supérieure, 2017.
- [80] F. Soleilhet, F. Benboudjema, X. Jourdain, and F. Gatuingt. Role of pore pressure on cracking and mechanical performance of concrete subjected to drying. *Cement and Concrete Composites*, 114:103727, 2020.
- [81] M. Thiery, V. Baroghel-Bouny, N. Bourneton, G. vilain, and C. Stéfani. Modélisation du séchage des bétons. Analyse des différents modes de transfert hydrique. *Revue européenne de génie civil*, 11(5):541–578, 6 2007.

- 831 [82] I. Vlahinić, H. M. Jennings, and J.J. Thomas. A constitutive model for drying of a
832 partially saturated porous material. *Mechanics of Materials*, 41(3):319–328, 2009.
- 833 [83] K.W. Wang and N.C. Pereira. Handbook of Environmental Engineering. In *Water*
834 *ressources in natural processes*, volume 4, 1986.
- 835 [84] I. Yurtdas, N. Burlion, and F. Skoczylas. Triaxial mechanical behaviour of mortar:
836 Effects of drying. *Cement and Concrete Research*, 34(7):1131–1143, 2004.